From Flow to Map in an Experimental High-Dimensional Electro-Optic Nonlinear Delay Oscillator

Laurent Larger,* Pierre-Ambroise Lacourt, Stéphane Poinsot, and Marc Hanna

UMR CNRS FEMTO-ST 6174/Optics Dpt, Université de Franche-Comté, 16 route de Gray, 25030 Besançon Cedex, France†

(Received 4 March 2005; published 21 July 2005)

An optoelectronic nonlinear delay oscillator seeded by a pulsed laser source is used to experimentally demonstrate a new transition scenario for the general class of delay differential dynamics, from continuous to discrete time behavior. This transition scenario differs from the singular limit map, or adiabatic approximation model that is usually considered. The transition from the map to the flow is observed when increasing the pulse repetition rate. The mechanism of this transition opens the way to new interpretations of the general properties of delay differential dynamics, which are universal features of many other scientific domains. We anticipate that the nonlinear delay oscillator architecture presented here will have significant applications in chaotic communication systems.

DOI: 10.1103/PhysRevLett.95.043903 PACS numbers: 42.65.Sf, 05.45.Jn, 42.82.Gw

Nonlinear delay differential equations (NLDDEs) with large delay have been the subject of growing interest in optics during the past 25 years [1–5]. This interest was first motivated by fundamental investigations of infinite phase space dynamics, which were easier to perform experimentally using optical and optoelectronics systems. Although dynamical systems of the same kind are encountered in various other fields, e.g., mechanics [6], or biology [7], experimental investigations in these fields are usually less reliable than in optics, and studies have been restricted to relatively difficult theoretical approaches or purely numerical investigations. Many of the corresponding setups for these systems are very well modeled using a simple first order (scalar) dynamical model:

$$\tau \frac{dx}{dt}(t) + x(t) = \lambda f(x(t - \tau_D)), \tag{1}$$

where $f(x)$ is a nonlinear function exhibiting usually at least one extremum, τ is a physical response time, τ_D is the delay, and λ is the weight of the nonlinear function in the dynamical process. The parameter λ is typically considered as the bifurcation parameter; i.e., increasing λ continuously from zero allows the observation of the well-known period-doubling bifurcation cascade. For the large delay case ($\tau/\tau_D = \varepsilon \ll 1$), these systems produce high complexity chaos and have recently found particular interest in secure optical communications [8–13], and, more generally, in chaos synchronization and control [14–17].

A common approach in the study of the numerous possible dynamical regimes for the large delay case ($\tau_D \gg \tau$) involves the so-called adiabatic approximation $\varepsilon(dx/dt) = 0$, sometimes also referred as the singular limit map [18]. This leads to the interpretation of the delay differential dynamical process as a discrete time mapping [$x_{n+1} = f(x_n)$], of the same class as the well-known logistic map [$x_{n+1} = \lambda x_n(1 - x_n)$], for which the unity iteration time step corresponds physically to the delay τ_D. This approach has led to good agreement with the flow model when focussing on the low-complexity regimes of NLDDEs (the first periodic regimes observed in the period-doubling cascade, i.e., for small λs). However, clearly different dynamical properties have been observed between the two models [19] when λ takes higher values corresponding to stronger nonlinear regimes, such as chaos or fast quasi-periodic oscillations. Specifically, these higher complexity dynamical regimes of the flow model exhibit fast fluctuations on time scales of the order of the rescaled response time τ/λ. This implies the presence of high frequency components that cannot be explained with the map model, yet which role is essential in the properties of the dynamics (high-dimensional chaotic behavior). In terms of chaotic attractor dimension, the flow model was found [20] to exhibit high dimensions proportional to $\lambda\tau_D/\tau = \lambda/\varepsilon$ [19,21] (as high as several hundred in real experimental situations). On the contrary, the map model intrinsically evolves in a one-dimensional phase space, thus not being able to produce such strong hyperchaotic flow dynamics.

Another noticeable difference between the mapping and the differential behavior concerns the so-called periodicity windows of the bifurcation diagram. In the map case, those windows are located along the λ axis after the fully developed chaotic regimes. Under the same parameter conditions in the flow case, no similar periodicity windows with a time step τ_D (the time scale in the flow corresponds to the map iteration step) are observed. Specific periodic regimes are, however, found for the flow case, but involving short time scale oscillations of the order of τ, referred to as higher harmonic periodic regimes [22], in contrast to the first low-complexity periodic regimes characterized by the long time scale τ_D.

In this Letter, we report an experimental setup which allows us to experimentally investigate a real map behavior with a different approach than the ''thought experiment'' consisting of the singular limit map. Typical periodicity windows are clearly seen as a signature of the discrete time characteristic. The setup will be interpreted as an intermediate situation between a one-dimensional map and an infinite dimensional flow. It will be finally shown that with

a proper tuning of temporal parameters, a smooth transition from the map to the flow can be obtained.

Experimental Setup.—Figure 1 represents the experiment that has been performed to generate either a flow or a map, depending on the laser source at the input. It is organized as an optoelectronic feedback loop similar to the one used in a previous demonstration of multi-10 Gbit/s encoding and decoding system using a continuous time chaotic waveform [23]. It consists of: (i) A $LiNbO_3$ wideband (12 GHz) integrated electro-optic (EO) Mach-Zehnder (MZ) modulator, with a half wave voltage of $V_\pi = 4.5$ V. It performs the nonlinear transformation through a multiple extrema interference function. (ii) A fiber-pigtailed motorized variable optical delay line used to finely tune the total feedback delay τ_D. (iii) A fast photodiode (10 GHz bandwidth) preamplified with a high-gain transimpedance amplifier (sensitivity 2.2 V/mW). (iv) An rf electronic driver with 18 dB gain, 26 dBm saturation output power, and 30 kHz–25 GHz bandwidth. Its output serves as a feedback signal applied to the rf electrodes of the MZ modulator. (v) For the observation of map behavior, the setup is seeded by a 10 ps pulsed fiber laser operating at 1.55 μm, with tunable repetition rate ($F_r = 1/T_r = 2.5$–10 GHz). The average optical power I_0 injected in the nonlinear delay oscillator can be adjusted with a pigtailed variable attenuator from 0 to 0.5 mW allowing for the tuning of the net feedback gain and enabling scanning of several dynamical regimes. (vi) When switching to a flow behavior, the pulsed laser source is replaced by a standard cw distributed-feedback semiconductor laser. This configuration in fact represents the most common architecture reported in the literature for studying nonlinear delay differential dynamics. Note that when the pulse laser repetition rate is far beyond the oscillator electronic cutoff frequency, only the mean intensity of the laser source is relevant, and the pulsed and cw setups are in fact equivalent.

The dynamical behavior of the MZ optical output is observed at the fiber coupler output, which is connected to a fast repetitive sampling oscilloscope equipped with a dc 30 GHz optical-to-electrical convertor. In the mapping configuration (with the pulsed laser source), bifurcation diagrams are measured using the following procedure. When triggered by the same rf clock used to mode lock the fiber laser, the sampling nature of the oscilloscope does not allow direct measurement of time series; however, histograms, or probability density functions (PDF) of the dynamical variable can be readily measured. With selection of a time window around the pulse center and with sufficiently long (a few seconds) acquisition time, an accurate $\mathrm{PDF}_\lambda(x)$ can be obtained. By repeating this operation for each stepwise increasing value of the optical power (i.e., increasing λs), a bifurcation diagram can be obtained within minutes.

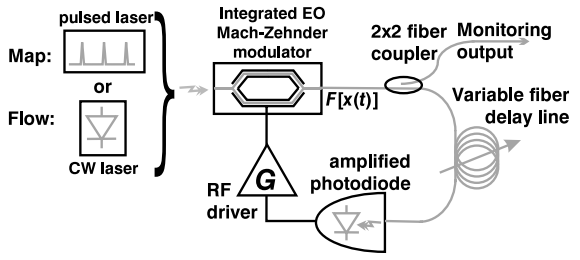

FIG. 1. Experimental setup.

Theory of operation and modeling of the map experiment.—The dynamical behavior of the oscillation loop is described as follows. When an optical pulse of power I_0 enters the MZ modulator, its intensity is modulated by the voltage $v(t)$ applied to the modulator at time $t = nT_r$. The normalized modulation function is the nonlinear transfer curve $F(x) = \sin^2[x + \Phi_0]$ corresponding to a two wave interference function with unity contrast; the parameter Φ_0 is tuned in practice by adjusting the bias at the dc electrode of the Mach-Zehnder modulator. The normalized dynamical variable is proportional to the MZ rf input voltage, and is defined as $x(t) = \pi v(t)/(2V_\pi)$. The modulator output intensity is converted to an electrical signal by an amplified photodiode followed by the rf driver. The nonlinearly EO modulated optical pulse is thus converted into an electrical pulse, the amplitude of which is determined by both a conversion factor A (in V/mW), and by electronic saturation effects depending on the optical pulse amplitude. The electrical pulse as compared to the optical pulse width is also affected due to the impulse response of the electronic feedback. This response is essentially determined by the photodiode, which is the slowest electronic component. The electrical pulse width at half maximum applied to the MZ electrode can be measured in open loop operation; it is found to be 40 ps, a value 4 times larger than the optical pulse width. The tunable optical delay line (resolution 4 fs) is adjusted experimentally so that the peak of the electrical feedback pulse is synchronized with the incoming short optical pulse inside the MZ modulator: this is achieved when the feedback delay matches an integer multiple of the repetition rate ($\tau_D = NT_r$). The integer N can be viewed as the memory size of the oscillation loop; it is directly related to the dimension of the system (in the experiment $\tau_D = 42$ ns, and $T_r = 200$ ps at 5 GHz, thus leading to $N = 210$). It corresponds to the number of independent initial conditions that are required to determine uniquely the normalized optical pulse amplitude sequence $\{p_n\}_{n\in\mathbb{N}}$, or the normalized electrical pulse sequence $\{x_n\}_{n\in\mathbb{N}}$ as well. Since the optical pulse is much shorter than the electrical feedback pulse, the former forces a sampling of the latter, at the repetition rate F_r. When the optoelectronic feedback impulse response width is shorter than the repetition period T_r, two successive optical pulses are modulated independently; the single order discrete time characteristic of the dynamics is a straightforward consequence of such a condition (each of the N successive

x_n depends on each N previous $x_{(n-N)}$ respectively). Increasing the impulse response time or increasing the repetition rate, would lead to a multiple order iteration process (x_n depends on $x_{(n-N)}, x_{(n-N-1)}, \ldots$). Thus, moving progressively to higher order iteration processes can be viewed as a practical way to observe a smooth transition from a map behavior to a flow behavior.

Assuming $\{h_n\}_{n\in\mathbb{N}}$ as the infinite impulse response of the electronic feedback sampled at the repetition rate of the pulse laser, and taking into account the nonlinear transformation resulting from the MZ and from the electronic saturation, the discrete time dynamics of the optical and electrical pulse amplitudes can be described as follows:

$$p_n = \lambda \sin^2\left[\sum_{k=0}^{\infty}(h_k x_{n-N-k}) + \Phi_0\right] \tag{2}$$

$$x_n = \frac{p_n}{1 + p_n/p_{\text{sat}}}, \tag{3}$$

where the normalized bifurcation parameter is $\lambda = \pi A I_0/(2V_\pi)$. Equations (2) and (3) are used to calculate, after transient removal and for N random initial values, the PDF of any dynamical regime. Each dynamical regime corresponds to a given λ (adjusted experimentally through the input optical pulse power), and to a given Φ_0 (adjusted experimentally through the MZ bias voltage). The coefficients $\{h_k\}$ are evaluated according to an open loop experimental record of the electrical pulse amplitudes corresponding to the detection of the unmodulated optical pulses. At $F_r = 5$ GHz, we obtained $\{h_k\} = \{+1; +0.0152; -0.0087; -0.0098; +0.0044; +0.0044; -0.000045\ldots\}$. Because of the wide frequency band of the electronics, the impulse response is in practice well approximated by a first order iteration process. Indeed, taking into account the second and the third coefficients does not lead to significant qualitative changes in the bifurcation diagram. This implies that the dimension of the iteration process actually corresponds to the number N of consecutive pulse amplitudes that are needed to fill the delay memory of the discrete time oscillator.

Results.—A wide range of different behavior can be observed depending on the values of λ and Φ_0. The values of Φ_0 corresponding to the bifurcation diagrams shown in Fig. 2 have been chosen because they clearly show a period-three window after the first chaotic regimes; this behavior is indeed of particular interest in nonlinear dynamics theory when looking for chaotic regimes [24,25]. Such a distinct period-three feature was obtained with $\Phi_0 \simeq 1.6$ (other nearby values also lead to the period-three window), within the experimentally available range of λ. Figure 2 (left) shows numerical bifurcation diagrams. The main picture was obtained from Eqs. (2) and (3), and the inset corresponds to a numerically simulated flow as described by Eq. (1). As already stated, the flow model does not exhibit any distinct periodic window inside the chaotic regime range. In contrast, under similar conditions the map model shows a large period-three window between $\lambda = 6.5$ and $\lambda = 7$. Such numerical diagrams are to be compared with the experimental ones depicted in Fig. 2 (right), the main diagram corresponding to the setup in Fig. 1 with the pulsed laser source, and the insert serving as a reference for the continuous time setup. The good agreement between the numerical and experimental diagrams, particularly in the position of the bifurcation points, validates the discrete time map adopted for the experiment modelling. It is to be noticed that the experimental flow diagrams [inset in Fig. 2 (right), corresponding to the cw laser seeding] does not exhibit any periodic window after the period-doubling cascade, as already underlined for the numerical simulation of the flow.

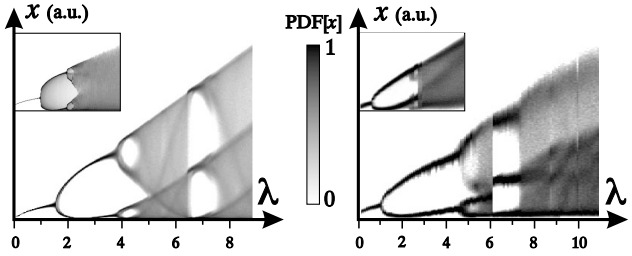

FIG. 2. Numerical (left) and experimental (right) bifurcation diagrams of the map behavior; the insets show the flow dynamics obtained when seeding the oscillator with a cw laser.

Other bifurcation conditions have been explored at different pulse repetition rates, namely, 2.5 and 10 GHz (Fig. 3). The period-three windows were also observed, even at 10 GHz for which each electrical pulse interacts with at least two successive optical incoming pulses due to the non-negligible impulse response of the electronic feedback loop. The 10 GHz diagram reveals, however, altered period-three windows, with noisy and broadened discrete level. One could thus suspect that increasing further the pulsed laser repetition rate would lead to more and more broadened discrete levels, thus merging together progressively the discrete levels, and making the diffuse period-three window vanish into a continuously distributed pulse amplitudes. The open loop electronic impulse responses shown in the inserts in Fig. 3 illustrates qualitatively the origin of the transition from a discrete time behavior to a continuous time one.

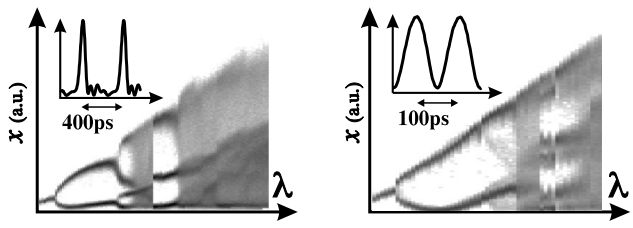

FIG. 3. Bifurcation diagrams at different repetition rates (left: 2.5 GHz, right: 10 GHz).

The particular mechanisms involved in the pulsed laser optoelectronic delay feedback setup suggest an interpretation of the transition from discrete to continuous time dynamical behavior. When the electronic feedback is faster than the repetition rate, two successive input pulses are independent, and any single pulse modulation is uniquely determined by the single Nth earlier pulse modulation. The oscillation loop time delay consists of N independent pulse amplitudes, resulting in an N-dimensional dynamical system, even if each iteration process is one-dimensional: the shortest correlation length in the produced pulse sequence is hence related to the delay. When the feedback impulse response in the oscillation loop is not fast enough with respect to the repetition rate, each single pulse has an influence on its following neighbors, thus introducing progressively a short time scale correlation, of the order of the impulse response width [corresponding to τ in Eq. (1)]: with an increasing repetition rate the dynamics is turning progressively from a discrete time process to a continuous time process.

Conclusion.—A discrete time nonlinear delay oscillator has been reported, which dynamical model has been established as a map. Several periodic and chaotic regimes have been observed, including a period-three window within the chaotic regime parameter range. The setup allows for the tuning of the various temporal parameters, such as the pulse repetition rate, the feedback delay, and the physical response time. Based on the physical principle of this setup, an interpretation of a possible mechanism in the transition from the discrete time behavior to the continuous time one has been proposed. This interpretation is formally related to the presence of a pulsed energy source seeding the oscillator, and verifying $pulse\ width < impulse\ response\ time < repetition\ rate < time\ delay$. It can thus be valid for the Ikeda ring cavity when seeded by a pulse laser as well, and for any other delay dynamics involved in biology, chemistry, mechanics, and exhibiting similar operating conditions. In the field of optics, the reported setup may find attracting application in chaos communication techniques through the use of Gbit/s symbolic dynamics encoding scheme [26,27], or chaos encryption schemes compliant with data packet formats.

This work was supported by the European Community (OCCULT project, IST-2000-29683), and by the French Ministry of Research (*Transchaos* project, ACI research program on Information and Security).

*Electronic address: laurent.larger@univ-fcomte.fr
†Also at GTL-CNRS Telecom / UMR CNRS FEMTO-ST 6174, 2–3 rue Marconi, 57070 Metz Cedex, France

[1] K. Ikeda, Opt. Commun. **30**, 257 (1979).
[2] H. M. Gibbs, F. A. Hopf, D. L. Kaplan, and R. L. Shoemaker, Phys. Rev. Lett. **46**, 474 (1981).
[3] A. Neyer and V. Edgar, IEEE J. Quantum Electron. **18**, 2009 (1982).
[4] T. Aida and P. Davis, IEEE J. Quantum Electron. **28**, 686 (1992).
[5] F. T. Arecchi, G. Giacomelli, A. Lapucci, and R. Meucci, Phys. Rev. A **45**, R4225 (1992).
[6] M. A. Johnson and F. C. Moon, Int. J. Bifurcation Chaos Appl. Sci. Eng. **9**, 49 (1999).
[7] M. Mackey and L. Glass, Science **197**, 287 (1977).
[8] C. R. Mirasso, P. Colet, and P. Garcia-Fernadez, IEEE Photonics Technol. Lett. **8**, 299 (1996).
[9] J.-P. Goedgebuer, L. Larger, and H. Porte, Phys. Rev. Lett. **80**, 2249 (1998).
[10] G. D. VanWiggeren and R. Roy, Science **279**, 1198 (1998).
[11] S. Sivaprakasam and A. K. Shore, Opt. Lett. **24**, 466 (1999).
[12] I. Fischer, Y. Liu, and P. Davis, Phys. Rev. A **62**, 011801(R) (2000).
[13] S. Tang and J. M. Liu, Opt. Lett. **26**, 1843 (2001).
[14] K. Pyragas,, Phys. Rev. E **58**, 3067 (1998).
[15] B. Mensour and A. Longtin, Phys. Lett. A **244**, 59 (1998).
[16] J. N. Blakely, L. Illing, and D. J. Gauthier, Phys. Rev. Lett. **92**, 193901 (2004).
[17] M.-Y. Kim, R. Roy, J. L. Aron, T. W. Carr, and I. B. Schwartz, Phys. Rev. Lett. **94**, 088101 (2005).
[18] B. Mensour and A. Longtin, Phys. Rev. E **58**, 410 (1998).
[19] M. Le Berre, É. Ressayre, A. Tallet, and H. M. Gibbs, Phys. Rev. Lett. **56**, 274 (1986).
[20] J. D. Farmer, Physica (Amsterdam) **4D**, 366 (1982).
[21] B. Dorizzi, B. Grammaticos, M. Le Berre, Y. Pomeau, É. Ressayre, and A. Tallet, Phys. Rev. A **35**, 328 (1987).
[22] K. Ikeda, K. Kondo, and O. Akimoto, Phys. Rev. Lett. **49**, 1467 (1982).
[23] N. Gastaud, S. Poinsot, L. Larger, M. Hanna, J.-M. Merolla, J.-P. Goedgebuer, and F. Malassenet, Electron. Lett. **40**, 898 (2004).
[24] T. Y. Li and J. A. Yorke, Am. Math. Mon. **82**, 985 (1975).
[25] Y. Liu and J. Ohtsubo, Opt. Commun. **93**, 311 (1992).
[26] S. Hayes, C. Grebogi, and E. Ott, Phys. Rev. Lett. **70**, 3031 (1993).
[27] S. D. Pethel, N. J. Corron, Q. R. Underwood, and K. Myneni, Phys. Rev. Lett. **90**, 254101 (2003).

Chaotic Breathers in Delayed Electro-Optical Systems

Y. Chembo Kouomou,[1,*] Pere Colet,[1] Laurent Larger,[2] and Nicolas Gastaud[3]

[1]*Instituto Mediterráneo de Estudios Avanzados IMEDEA (CSIC-UIB), Campus Universitat de les Illes Balears, E-07122 Palma de Mallorca, Spain*

[2]*UMR CNRS FEMTO-ST 6174/Optics Department, Université de Franche-Comté, 16 Route du Gray, 25030 Besançon cedex, France*

[3]*GTL-CNRS Telecom, UMR FEMTO-ST 6174, 2–3 rue Marconi, 57070 Metz cedex, France*

(Received 24 September 2004; published 9 November 2005)

We show that in integro-differential delayed dynamical systems, a hybrid state of simultaneous fast-scale chaos and slow-scale periodicity can emerge subsequently to a sequence of Hopf bifurcations. The resulting time trace thereby consists in chaotic oscillations "breathing" periodically at a significantly lower frequency. Experimental evidence of this type of dynamics in delayed dynamical systems is achieved with a Mach-Zehnder modulator optically fed by a semiconductor laser and is subjected to a delayed nonlinear electro-optical feedback. We also propose a theoretical understanding of the phenomenon.

DOI: 10.1103/PhysRevLett.95.203903 PACS numbers: 42.65.Sf, 05.45.Jn

Since the pioneering work of Ikeda [1], important experimental and theoretical research has focused on the dynamics of nonlinear optical systems with delayed feedback, and the so-called Ikeda equation has been converted into a paradigm for the study of differential-delay systems in physics. In particular, a wide variety of acousto-optical and electro-optical systems can be modeled with an Ikeda equation [2,3], or one of its modified versions. For example, some acousto-optical devices were modeled with an Ikeda-like equation containing higher-order differential terms [4], while in another setup, the limit case of a zero delay was studied [5]. In all cases, several types of instabilities and nonlinear behaviors have been evidenced and investigated, from bistability to hyperchaos. However, if a wide variety of *differential* delayed systems have been investigated, only a very limited interest has been paid until now to the nonlinear dynamics and bifurcation behavior of *integro-differential* delayed systems. Here, a quite interesting and unreferenced phenomenon can be observed: simultaneous fast-scale chaos and slow-scale periodicity.

In this Letter, the system under study corresponds to the experimental setup of Fig. 1. The electro-optical feedback loop is composed with several elements: a Mach-Zehnder modulator whose radio-frequency and dc half-wave voltages are V_π and $V_{\pi_{\rm dc}}$, respectively, biased with a voltage V_B and illuminated by a continuous-wave semiconductor laser source of power P, an optical fiber delay line of delay time T_D, a photodiode with gain g, and a radio-frequency amplifier with gain G to convert the optical feedback signal into an electrical voltage $V(t)$ for the Mach-Zehnder electrode. The overall attenuation of this feedback loop (delay line, connectors, etc.) is described in terms of the parameter A. The electronic bandwidth of the feedback loop is supposed in first approximation to result from two cascaded linear first-order low-pass and high-pass filters, with low and high cutoff frequencies f_L and f_H, respectively. If we consider $x(t) = \pi V(t)/2V_\pi$ as the dimensionless variable describing the system, its dynamics can be modeled by the following integro-differential delayed equation [6]:

$$x + \tau\frac{dx}{dt} + \frac{1}{\theta}\int_{t_0}^{t} x(s)ds = \beta\cos^2[x(t - T_D) + \phi], \quad (1)$$

where $\beta = \pi gAGP/2V_\pi$, $\phi = \pi V_B/2V_{\pi_{\rm dc}}$, $\theta = 1/2\pi f_L$, and $\tau = 1/2\pi f_H$. Here, the three time parameters of the system have quite different orders of magnitude. For numerical simulations, we work with values compatible with those of the experimental setup, that is, $\tau = 25$ ps, $T_D = 30$ ns, and $\theta = 5$ μs.

We can now analyze the dynamics of the system with respect to the feedback strength β (which is proportional to the feeder-laser power P) and the offset phase ϕ (proportional to the bias voltage of the Mach-Zehnder V_B). If we introduce the variable $y = \frac{1}{\tau}\int_{t_0}^{t} x(s)ds$, the evolution Eq. (1) may formally be rewritten as

$$\dot{y} = x, \qquad \dot{x} = -x - \epsilon y + \beta\cos^2(x_R + \phi), \quad (2)$$

where the overdot denotes the derivative relative to the dimensionless time t/τ. The dynamics of the system is now

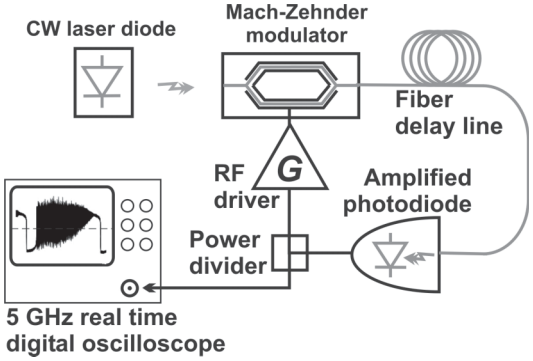

FIG. 1. The experimental setup.

ruled by two new dimensionless parameters. The first one is the ratio between the low and the high cutoff frequencies $\epsilon = \tau/\theta = 5 \times 10^{-6}$. The second one is the dimensionless delay $R = T_D/\tau = 1.2 \times 10^3$, which also roughly indicates the order of magnitude for the effective number of degrees of freedom attached to the system [6]. The flow of Eq. (2) has a single stationary point $(x_{st}, y_{st}) = (0, \frac{\beta}{\epsilon}\cos^2\phi)$, and the stability of this unique fixed point can be investigated through the eigenvalue equation

$$\lambda^2 + \lambda + \epsilon + \beta \sin 2\phi \lambda e^{-\lambda R} = 0. \quad (3)$$

It is known that a Hopf bifurcation may occur in the system when λ becomes pure imaginary, that is, when $\lambda = i\omega$. According to Eq. (3), the frequency ω of the limit cycle induced by the Hopf bifurcation should obey the nonlinear algebraic system

$$-\omega^2 + \epsilon + \gamma\omega \sin\omega R = 0, \quad (4)$$

$$1 + \gamma \cos\omega R = 0, \quad (5)$$

where $\gamma \equiv \beta \sin 2\phi$ is the relevant control parameter for the bifurcation. The solutions (γ_H, ω_H) of the above algebraic system give the critical value γ_H of the control parameter for which the fixed point turns unstable and bifurcates to a limit cycle of frequency ω_H. We can first uncouple Eqs. (4) and (5) to obtain independent equations for γ and ω following

$$1 + \gamma \cos\left[R\frac{(\gamma^2 - 1) \pm \sqrt{(\gamma^2 - 1)^2 + 4\epsilon}}{2}\right] = 0, \quad (6)$$

$$-\omega^2 + \epsilon = \omega \tan\omega R, \quad (7)$$

whose solutions may be approximated with an excellent precision as

$$\gamma_0 = -1 - \epsilon R/2, \qquad \omega_0 = \sqrt{\epsilon/R}, \quad (8)$$

on the one hand, and as

$$\gamma_k = (-1)^{k+1}\left[1 + \frac{(\epsilon R^2 - k^2\pi^2)^2}{2k^2\pi^2 R^2}\right], \qquad \omega_k = k\frac{\pi}{R}, \quad (9)$$

on the other, k being a stricly positive integer.

From Eq. (5), it clearly appears that the fixed point $x = 0$ is stable independently of R when $|\gamma| = |\beta \sin 2\phi| < 1$. In particular, it is interesting to notice that this trivial fixed point is stable independently of ϕ when $\beta < 1$. However, limit cycles of frequency ω_k may emerge when crossing the critical bifurcation value of their related counterpart γ_k (which is always such that $|\gamma_k| > 1$).

For positive γ, the first bifurcation occurs at $\gamma_1 = 1 + 2.5 \times 10^{-7}$, leading to the emergence of a limit cycle of frequency $\omega_1 = \pi/R$, corresponding to a period of $2T_D = 60$ ns. When γ is further increased, the fundamental frequency of that limit cycle remains constant, even though the waveform changes from a sinusoid to a quasi-square wave [7]. Numerical simulations show that starting from an initial condition corresponding to the stationary fixed point, the system always evolves to limit cycles of period $2T_D$ when γ is increased beyond 1 (see Fig. 2), and chaos is observed when γ is sufficiently high.

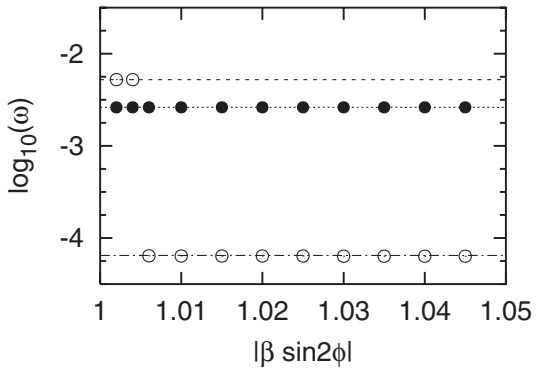

FIG. 2. Numerical variation of the limit cycles' frequencies after the Hopf bifurcations at $\gamma = -1$ (○), and after $\gamma = 1$ (●). The initial condition in the whole $[-T_D, 0]$ interval is the trivial fixed point. The three horizontal dashed lines, respectively, correspond from top to bottom to $\omega_2 = 2\pi/R$, $\omega_1 = \pi/R$, and $\omega_0 = \sqrt{\epsilon/R}$. Note that the frequencies found numerically always perfectly coincide with one of the three aforementioned analytical frequencies.

On the other hand, for $\gamma < 0$, the first limit cycle to emerge appears at $\gamma_2 = -1 - 9.1 \times 10^{-6}$ with a frequency $\omega_2 = 2\pi/R$, corresponding to a period of $T_D = 30$ ns. But in this case, when γ is increased in absolute value and reaches the value $\gamma_0 = -1.003$, the limit cycle of frequency $\omega_0 = \sqrt{\epsilon/R}$ emerges and becomes the

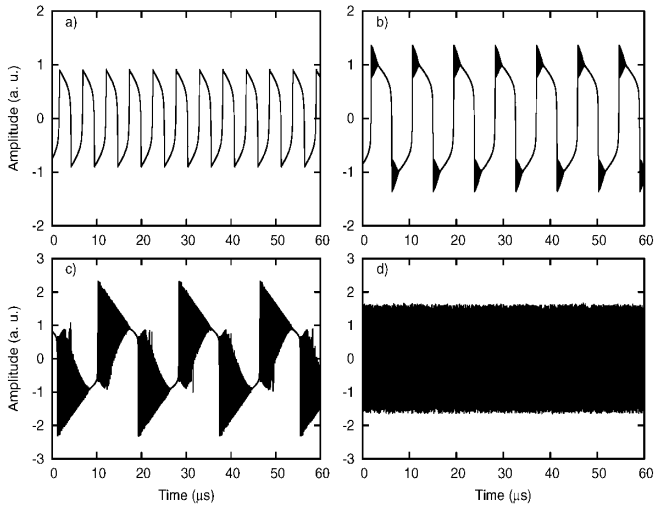

FIG. 3. Birth, evolution, and destruction of the breathers as the nonlinear feedback strength parameter β is increased, when $\phi = -\pi/4$ (symmetric case). (a) $\beta = 1.5$. (b) $\beta = 2.0$. (c) $\beta = 3.0$. (d) $\beta = 3.5$.

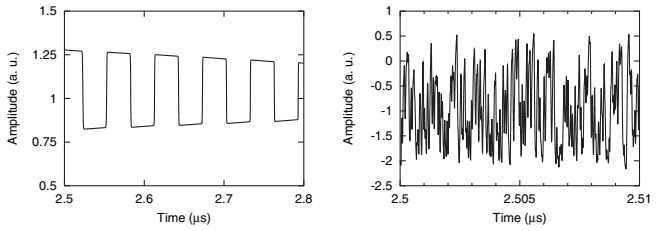

FIG. 4. Inner structure of the breathers (fast-scale dynamics). (a) Enlargement of Fig. 3(b) ($\beta = 2$): the breathers are $2T_D$ periodic. (b) Enlargement of Fig. 3(c) ($\beta = 3$): the breathers are chaotic.

attracting limit cycle when the initial condition is taken near the unstable fixed point. Effectively, the frequency of the system's oscillations switches beyond γ_0 from ω_2 to ω_0, *which is approximately 100 times smaller.* Figure 2 clearly indicates this drastic change of time scale: while we have oscillations of period $T_D = 30$ ns when $\beta \sin 2\phi = -1.001$, we rather have oscillations of period ~ 3 μs when $\beta \sin 2\phi = -1.01$. The emergence of a stable limit cycle whose period is significantly greater than τ and T_D opens the way to a very interesting phenomenology.

Effectively, when β is increased subsequently to the secondary bifurcation at $\gamma = \gamma_0$, we can witness the arising of a hybrid regime where a fast-scale dynamics is superimposed onto the slow-scale limit cycle. For example, it can be seen in Fig. 3(a) that when β is increased to 1.5, the amplitude extrema begin to behave *locally* like paired fixed points, in the sense that the dynamics becomes significantly slow at their neighborhood. As β is further increased, quasi-square-wave oscillations of period $2T_D$ emerge at their vicinity, but as can be seen in Fig. 3(b) they are rapidly damped just after their birth, that is, as soon as the system moves away from an extremum: we refer to them as *breathers,* and, at this stage, these breathers are still periodic. The internal frequency and the exponential damping of the emerging breathers can also be estimated analytically. In fact, at this early stage, the mean value contribution of the feedback term $\beta \cos^2(x_R + \phi)$ in Eq. (2) is canceled by the mean value of filter term ϵy, whose fluctuating component is negligible. Therefore, the extrema $\tilde{x}_{\rm st}$ of the low-frequency oscillation coincide with a good approximation to the solutions of the transcendental algebraic equation $x = \frac{1}{2}\beta \cos 2(x + \phi)$. Then we can track the evolution of a perturbation $\delta\tilde{x} = \delta\tilde{x}_0 e^{(\tilde{\kappa} + i\tilde{\omega})t}$ around the extrema $\tilde{x}_{\rm st}$, and it is found that the breathers emerge with a winding frequency $\tilde{\omega} = \pi/R$, and are damped at a rate $\tilde{\kappa} \simeq \ln(\tilde{\gamma})/R$, with $\tilde{\gamma} = \beta \sin 2(\tilde{x}_{\rm st} + \phi)$. When β is increased, the fluctuating component of the term ϵy also increases, and it can be calculated from a multiple time scale analysis (using ϵ as the expansion parameter) that, as a consequence, the damping drops to $\tilde{\kappa} \sim -\epsilon^{-1}$; i.e., the breathers begin to span over a time scale of the order of θ.

When β continues to increase, the breathers become chaotic, as can be seen in Fig. 3(c). Here, we are in front of a hybrid regime where the chaos is triggered at a ns time scale and superimposed onto the low-frequency limit cycle whose period is of the order of a few μs. In Fig. 3(d), it is shown that a further increase of β leads to the destruction of the breathers and to chaotic oscillations without any trace of slow-scale dynamics. In Fig. 4, we can see the inner structure of the breathers of Fig. 3. The enlargement of Fig. 4(a) shows the quasi-square-wave $2T_D$-periodic structure of the breathers of Fig. 3(b), in accordance to the winding frequency $\tilde{\omega} = \pi/R$ predicted by the theory, while Fig. 4(b) displays the fast-scale chaotic nature of the breathers shown in Fig. 3(c).

This dynamical behavior has also been recovered experimentally. In the experimental setup, the electro-optical modulator is a 10 GHz commercial $LiNbO_3$ integrated Mach-Zehnder modulator with $V_{\pi_{\rm dc}} = 4.0$ V and $V_\pi = 4.2$ V. The coherent optical feeder of this modulator is a distributed feedback semiconductor laser emitting at the standard infrared wavelength of 1550 nm. The delay line is a 6 m long single-mode optical fiber yielding an overall time delay of 30 ns. The wide-band amplified photodetector has a sensitivity of 2 V/mW and a 10 GHz bandwith. The radio-frequency electronic driver SHF100CP has a bandwidth ranging from 30 kHz to 25 GHz, and it performs within the nonlinear feedback loop an amplification whose gain is 18 dB (26 dBm at 1 dB compression). The amplitude of the background random noise of the experimental setup has been measured in the $\beta < 1$ regime (small feedback gain, when the fixed point $x = 0$ is a stable solution), and it is typically from 20 to 30 times smaller than the amplitude of the breathers which are obtained experimentally.

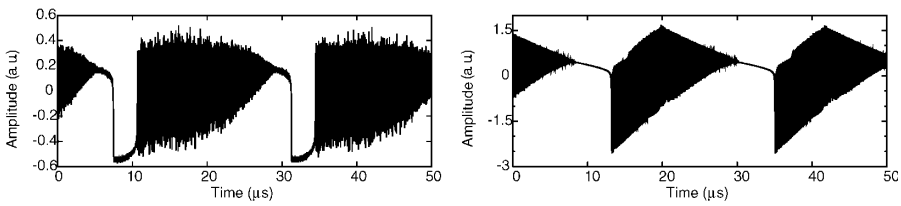

FIG. 5. Large-scale time traces of the hybrid regime of simultaneous slow-scale periodicity and fast-scale chaos. Adjacent asymmetrical breathers can also merge as they are growing. (a) Experimental time trace, with $P = 4.15$ mW and $V_B = 3.09$ V. (b) Numerical time trace, with $\beta = 2.8$ and $\phi = -\pi/10$.

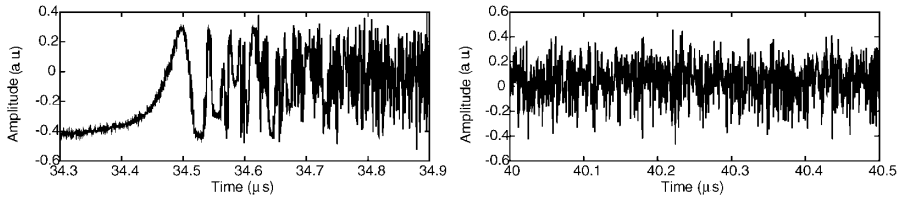

FIG. 6. Small-scale experimental time traces [enlargement of Fig. 5(a)]. (a) Onset of chaos in the breathers. Transients associated with the time delay T_D can clearly be identified. (b) Fully developed chaos within the breathers.

Figure 5(a) presents the experimental large-scale time traces corresponding to the chaotic breathers, and Fig. 5(b) displays the related numerical simulation. These experimental breathers correspond to the most general case of *asymmetric* breathers (obtained when $\phi \neq -\pi/4$), by opposition to the breathers of Fig. 3(c) which were *symmetric* relative to the horizontal axis ($\phi = -\pi/4$). In Fig. 6, an enlargement of the experimental time traces is displayed, and it enables one to have a better insight into the underlying mechanism of the process. The onset of chaos at the beginning of each breather is shown in Fig. 6(a). The transients related to the time delay T_D can clearly be recognized. Enough time is provided for these transients to evolve towards fully developed chaos as can be seen in Fig. 6(b), and therefore the occurrence of this phenomenon is not only related to the integro-differential dynamical property of the feedback loop, but also to the ratio between the different time scales of the system.

To the best of our knowledge, it is the first time that chaotic breathers are identified in a delayed dynamical system, even though it is known that chaotic breathers can exist in systems of ordinary differential equations. For example, they have been encountered in N-dimensional nonlinear systems with many time scales, where the nonlinearity is topologically present in a single direction of the state space: in that context, they emerged as the consequence of a nonlinear combination of $N-1$ oscillation modes, the so-called full instability regime [8]. Chaotic breathers have also been met in nonlinear systems excited by a high frequency forcing term modulated in amplitude by a slowly varying quasiperiodic envelope [9]. In our case, chaotic breathers appear as a new solution in autonomous and delayed dynamical systems, a robust and stable intermediate state between periodicity and full chaos.

In conclusion, this study has evidenced that in delayed dynamical systems, fast-scale chaos can coexist with slow-scale periodicity. We have shown that this phenomenon can be observed in a relatively simple model, as the result of the interplay between a bandpass filter and a nonlinear feedback delay term. In systems where the filter is only low pass (and not bandpass) as in the Ikeda model, fast-scale chaos is observed when the feedback strength is high enough; however, slow-scale periodicity (breathers) can definitively not arise. The disparity between the various time scales should also be emphasized, as in our case, for example, they span over 6 orders of magnitude. Neuronal systems also typically present a wide diversity of time scales in their dynamics, and they can display a large variety of spiking and bursting behaviors that are ruled by nonlinear evolution equations similar to the flow (2) [10]; if the propagation delay were taken into account in such models, we could expect chaotic breathers to appear. In general, depending on the ratios between their related time scales, coexistence of chaos and periodicity could also be observed in other delayed dynamical systems, provided that the delayed feedback signal is subjected to a kind of bandpass filtering.

This work has been funded by European Commission (project Occult, IST-2000-29683). Y. C. K. and P. C. acknowledge financial support from MEC (Spain) and FEDER (Grants No. FIS2004-00953, No. BFM2001-0341-C02-02, and No. TIC2001-4572-E). Helpful discussions with R. Herrero, G. Orriols, C. R. Mirasso, and M. Matías are acknowledged. Y. C. K. also acknowledges a research grant from the *Govern de les Illes Balears.*

*Corresponding author.
Electronic address: ckyanne@imedea.uib.es

[1] K. Ikeda, Opt. Commun. **30**, 257 (1979).
[2] A. Neyer and E. Voges, IEEE J. Quantum Electron. **18**, 2009 (1982).
[3] R. Vallée and C. Delisle, Phys. Rev. A **34**, 309 (1986).
[4] R. Vallée, P. Dubois, M. Côté, and C. Delisle, Phys. Rev. A **36**, 1327 (1987); R. Vallée and C. Mariott, Phys. Rev. A **39**, 197 (1989).
[5] F. A. Narducci, D. W. Bromley, G.-L. Oppo, and J. R. Tredicce, Opt. Commun. **75**, 184 (1990).
[6] J.-P. Goedgebuer, P. Levy, L. Larger, C.-C. Chen, and W. T. Rhodes, IEEE J. Quantum Electron. **38**, 1178 (2002); N. Gastaud, S. Poinsot, L. Larger, J.-M. Merolla, M. Hanna, J.-P. Goedgebuer, and F. Malassenet, Electron. Lett. **40**, 898 (2004).
[7] T. Erneux, L. Larger, M. W. Lee, and J.-P. Goedgebuer, Physica (Amsterdam) **194D**, 49 (2004).
[8] J. Rius *et al.*, Phys. Rev. E **62**, 333 (2000); Chaos**10**, 760 (2000).
[9] Z. Qu, G. Hu, G. Yang, and G. Qin, Phys. Rev. Lett. **74**, 1736 (1995).
[10] E. M. Izhikevich, Int. J. Bifurcation Chaos Appl. Sci. Eng. **10**, 1171 (2000), and references therein.

Nonlinear Dynamics - a primer

Lucas Illing

1 Nonlinear Dynamics

In nonlinear dynamics we study, in principle, any system that can't be described by linear equations. This is of course about everything and it is like saying we study "nonelephant animals". Clearly, in the end, we have to focus on some specific systems to make headway. Nevertheless, the main goal of nonlinear dynamics is to look at descriptions of physical, chemical, biological, and technical systems in ways that are universal, broadly applicable, and predictive.

My goal is to quickly run through a few universally applicable concepts from nonlinear dynamics that will help us to understand the experiment.

2 Model

The system we deal with can (most likely) be pretty accurately described by a very difficult to study delay-differential equation. However, if we focus on the main feature of interest, the variation of the amplitude of the pulse circulating in the feedback loop, we can write down the following much simpler map model.

$$x_{n+1} = f_{\mathrm{nl}}(x_n) = \lambda \sin^2(x_n + \varphi_0) \tag{1}$$

The variable x_n denotes the ampliude of the nth pulse, φ_0 the phase that is set through the Mach-Zehnder bias voltage, and λ the feedback strength that can be adjusted by varying the pulse height of the electric signals send from the function generator to the laser.

3 Solutions, Transients, Attractors

Ok, we have a model, what now? In your physics education so far you have mainly encountered problems that can be solved in the best sense we know of. That is to say, we are often able to write down an analytic solution in terms of known functions such as sine and exponential functions. Such analytic solutions tell us the state of a system at any arbitrary position and arbitrary time t. Typically we have to specify some initial condition or boundary condition, but that's it. There exists a unique solution and we can write it down.

In general, this is asking too much. For example, for many chaotic solution it is very apparent that requiring an expression consisting of known functions to tell us the state of a system for arbitrary t is not possible. Chaotic solutions are non-periodic, thus a solution in terms of a finite series of periodic functions will not suffice. In addition, chaos is characterized by extreme sensitivity to initial conditions, meaning that a small change in the way the system is started will after an exponentially short time result in a big change. Thus, the initial conditions enter in a non-trivial way.

In nonlinear dynamics we are therefore often satisfied with results that tell us, for example, whether the system will typically and in the long term be performing periodic oscillations or reach an equilibrium.

Think of a damped pendulum. The precise motion of the pendulum will vary depending on the initial position and initial speed. However, in the long term, the pendulum will always end up hanging straight down. This equilibrium point is called an *attractor* because it is the end point of all solutions except for the one associated with the initial condition where the pendulum is pointing exactly upward. This second, unstable equilibrium point of the pendulum is not attracting anything nor can it be observed in experiment (due to noise).

Nonlinear dynamics provides techniques to find and classify final states, such as the straight up and straight down solutions of the pendulum, without worrying about the many ways that these states are reached. That is, we typically do not worry about *transients*, a term describing the solutions that connect the initial condition and the limit set (attractor) that is reached in the $t \to \infty$ limit.

Another important term we need is *bifurcation*. What is that? A bifurcation occurs when the qualitative behavior of the system changes as a system-parameter is varied. For example, as the feedback gain is increased a system might go from a steady state solution to an oscillatory solution or the period of the oscillatory solution may suddenly double as a parameter threshold is crossed.

4 Sine Square Map - Numerics

A common way to visualize nonlinear maps is by plotting the current value x_n versus the next value $x_{n+1} = f_{\rm nl}(x_n)$ as shown in Fig. 1. This allows a graphical solution. Start with the initial point x_0 on the horizontal axis (here $x_0 \sim 2.8$) and draw a vertical line until you intersect the nonlinear function. This is your next value x_{n+1}. Now draw a horizontal line until you hit the 45 degree line ($x_{n+1} = x_n$). This makes the result of the calculation you have just performed the starting point for your next calculation. For the next iterate, start again by drawing a vertical line until you hit $f_{\rm nl}(x_n)$. Doing this a few times you can often quickly figure out whether the map converges to some point or not.

In Fig. 2 we plot the attractors of the sine-square map but do not plot the transient any more because we are not interested in it. Why are we not interested? Consider the experiment, by the time we measure something with the oscilloscope hundreds of millions of pulses have

circulated in the feedback loop. Clearly, if the experimental system does converge to an attractor it already has by the time we have a chance to look at it.

The upper left panel of Fig. 2 corresponds to Fig. 1 with a value for $\lambda = 1.2$. It is seen, that if the feedback parameter λ is increased, the final attracting state is not anymore a single point but first an alternating succession of two distinct points (period 2), then four distinct points (period four), then eight distinct points (period eight), ... Finally we reach a very complicated attractor, a chaotic attractor. Each time the attractor changes from one behavior to the next, e.g. from period two to period four oscillations, a bifurcation has taken place. In this case a so called period doubling bifurcation (sometimes also called flip bifurcation). The succession of bifurcations observed in this map is called period doubling route to chaos and was first observed and analyzed by Feigenbaum [1, 2].

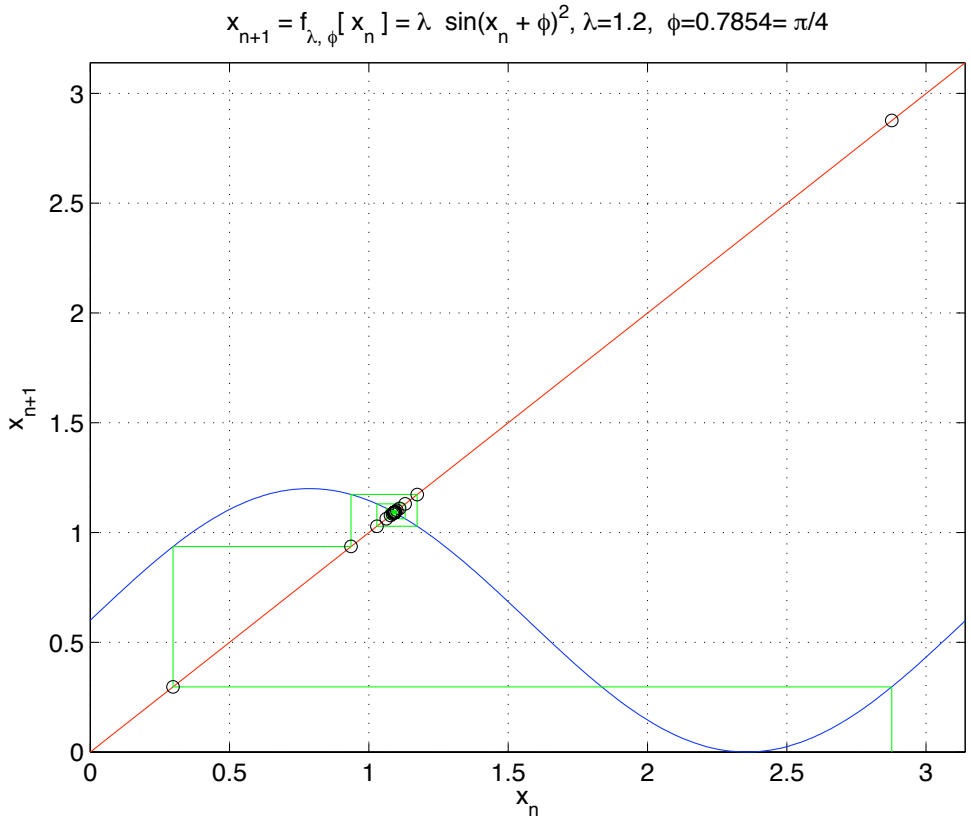

Figure 1: Cobweb diagram showing the transient solution as it converges to a fixed point attractor.

It is the purpose of this experiment to measure these bifurcations and to thereby introduce you to some fundamental notions used to analyze nonlinear systems. This is in addition to letting you work with the awesome fiber-optics equipment that has been developed by the telecommunications industry over the past decade and the super-fast electronics that go with it.

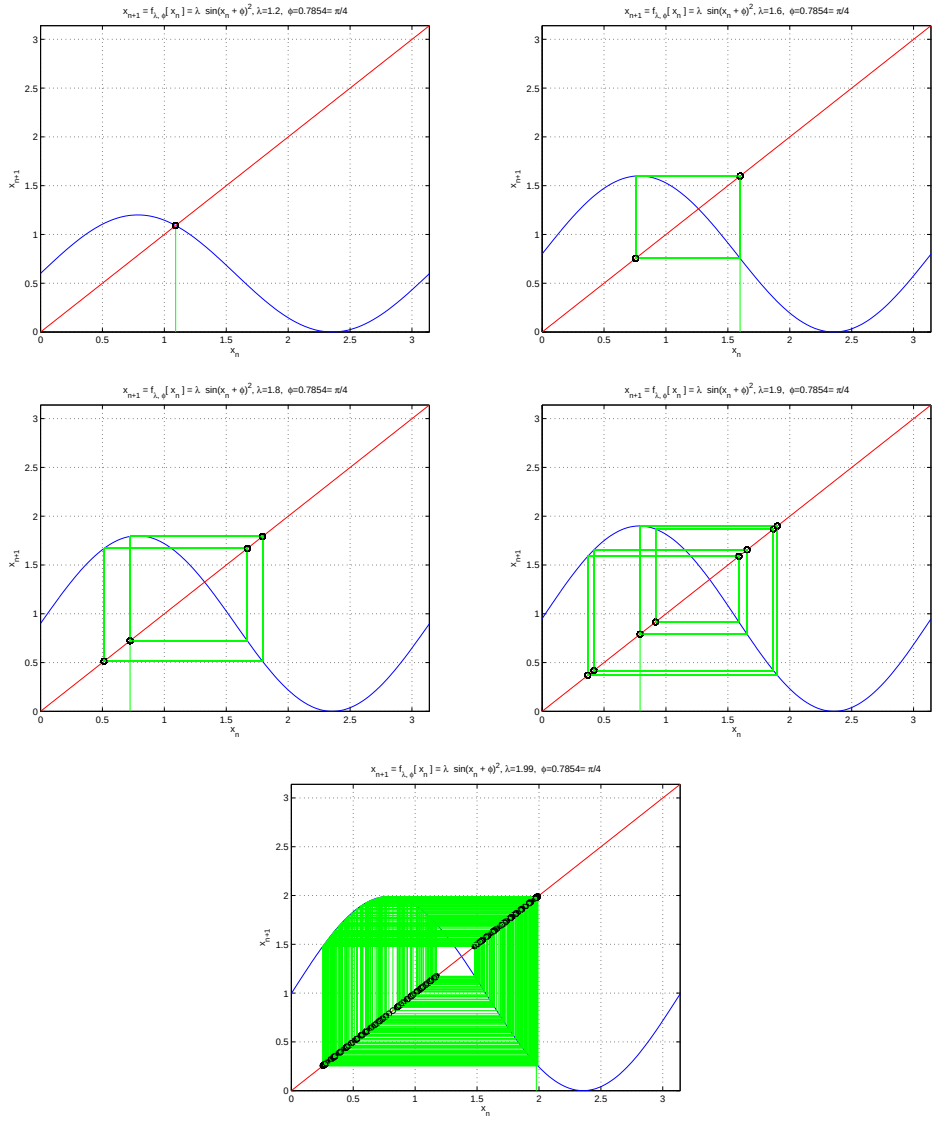

Figure 2: Cobweb diagram showing the period doubling route to chaos ($\lambda = 1.2$; 1.6; 1.8; 1.9; 1.99 and $\varphi_0 = \pi/4$).

As we have seen, what we really are interested in are the bifurcations and the final attractor. Therefore, instead of plotting a different figure for each new parameter value it is convenient to show the the x-values of the points forming the attractor versus the bifurcation parameter λ. The result is the bifurcation diagram shown in Fig. 3. Pretty right?

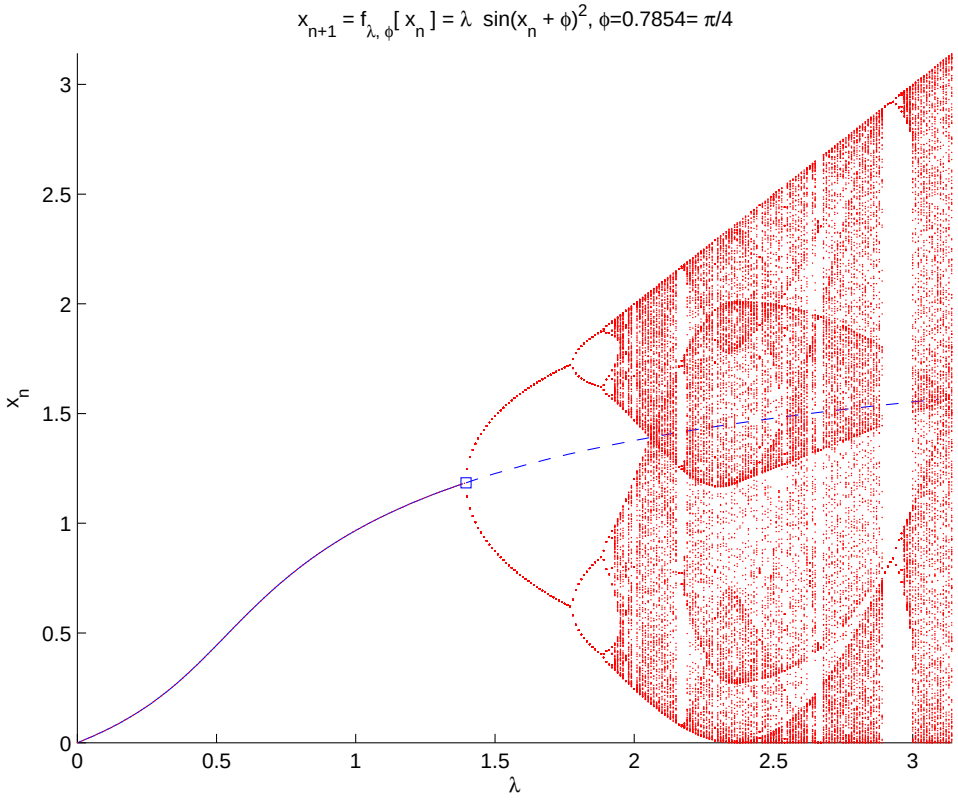

Figure 3: Bifurcation Diagram for sine-squre map with $\varphi_0 = \pi/4$

5 Sine Square Map - Analytics

Now nonlinear dynamics is not about showing pretty pictures but mathematical analysis. Many features of the bifurcation diagram (Fig. 3) can be explained using rigorous and at times quite sophisticated mathematics. To get a flavor of this let us start with the simplest task. We are going to find the first bifurcation point at $\lambda \approx 1.39577$.

We will focus here on the case $\varphi_0 = \pi/4$. Note that this is not necessarily the correct value for the conditions in your experiment. So one option for the report is to determine a realistic value for φ_0 and see what the bifurcation diagram looks like for that value.

5.1 Period 1 solution

In any case, assume $\varphi_0 = \pi/4$. We first look for period 1 solutions, that is solutions for which $x_n = x_{n+1} = x^*$.

$$x^* = \lambda \sin^2(x^* + \pi/4) \tag{2}$$

Eq. (2) is hard to solve, if we are trying to find a solution $x^*(\lambda)$. So instead we turn the diagram on its head and plot

$$\lambda = \frac{x^*}{\sin^2(x^* + \pi/4)} \tag{3}$$

The period 1 solution given by Eq. (3) is shown by the blue line in Fig. 3.

5.2 Stability of period 1 solution

As we have seen on the example of the pendulum, the $t \to \infty$ limit set solutions can be either stable (attracting), such as the solution where the pendulum is hanging straight down, or unstable (repelling), as for the case where the penulum points straight upward.

To determine the stability property of a solution it is enough to consider small perturbations around the solution, *i. e.* consider $x^* + \delta_n$. Due to δ_n being small we can linearize the map:

$$x^* + \delta_{n+1} = f_{\rm nl}(x^* + \delta_n) \approx f_{\rm nl}(x^*) + \left.\frac{df_{\rm nl}(z)}{dz}\right|_{z=x^*} \delta_n + \ldots \tag{4}$$

Since $x^* = f_{\rm nl}(x^*)$ this simplifies to the following linear map,

$$\delta_{n+1} = f'_{\rm nl}(x^*)\, \delta_n, \tag{5}$$

where we have used $f'_{\rm nl}(x^*)$ as shorthand notation for $df_{\rm nl}(z)/dz|_{z=x^*}$. Our goal is now to find out whether this linear map leads to solutions δ_n that decay to zero as $n \to \infty$ in which case the x^*-solution is stable. If the δ_n grow then x^* is unstable. In other words if the absolute value of the slope of the nonlinear function is less than one

$$|f'_{\rm nl}(x^*)| < 1, \tag{6}$$

then $x^*$is stable. If it is larger than one x^* is unstable.

In our particular case, Eq. (6) implies that we need to satisfy the condition

$$|2\lambda \cos(x^* + \pi/4) \sin(x^* + \pi/4)| < 1 \tag{7}$$

What we are really interested in is whether and if so when the solution switches from being stable to being unstable. Thus we can make our life easier by finding values for λ where

$$|2\lambda \cos(x^* + \pi/4) \sin(x^* + \pi/4)| = 1 \tag{8}$$

Therefore we combine Eq. (8) and the equation relating λ and x^* [Eq. (3)] and we solve the following equations numerically

$$\pm 1 = 2x^*_{bif}\cot(x^*_{bif}+\pi/4) \quad (9)$$

$$\lambda_1 = \frac{x^*_{bif}}{\sin^2(x^*_{bif}+\pi/4)} \quad (10)$$

to obtain as the only real solution (non imaginary solution)

$$x^*_{bif} = 1.18475 \qquad \lambda_1 = 1.39577 \quad (11)$$

This bifurcation value is shown as a blue square in Fig. 3. Without further proof, we can assert by looking at the numerics, that the period 1 solution is stable for $\lambda < 1.39577$ (solid blue line) and unstable for $\lambda > 1.39577$ (dashed blue line).

5.3 Beyond period 1

One can now attempt to continue in the same manner. Find the period 2 solution (or potentially several period 2 solutions) and then determine when this solution is stable. That is, one would need to solve the coupled nonlinear equation

$$x^*_1 = f_{\rm nl}(x^*_2) \quad (12)$$

$$x^*_2 = f_{\rm nl}(x^*_1) \quad (13)$$

This becomes tedious very quickly. If we were to do it we would find that the period 2 solution is created (comes into existence) just as the period 1 solution becomes unstable, *i. e.* for $\lambda_1 = 1.39577$. Thus λ_1 is a bifurcation point. Then the period 2 solution turns from stable to unstable just as the period four solution comes into existence. It is seen from Fig. 3 that these bifurcations take place for smaller and smaller increases of λ. Indeed the limit where all periodic orbits with periods $1, 2, 4, 8, \ldots, \infty$ have been created and have become unstable is reached for a finite value of the bifurcation parameter (λ_∞). At this point a chaotic attractor exists. Note that coexisting with this attractor and densely embedded in it are all the unstable (and repelling) periodic solutions that have been created in the period doubling cascade.

This is your very brief introduction to chaos and should give you a glimpse of what is going on in the experiment. Realistically we can not expect to be able to measure the bifurcations much beyond the period 4 orbit, because noise will smear out the bifurcation diagram.

6 Universality

So what is universal about all of this? For one, it turns out that the period doubling route to chaos is observed in many systems. So having studied it in one example allows one to recognize and analyze it in other systems.

However, universality goes much deeper. If we denote the parameter values at which the nth bifurcation takes place by λ_n then the following limit exists

$$\delta = \lim_{n\to\infty} \frac{\lambda_{n+1} - \lambda_n}{\lambda_{n+2} - \lambda_{n+1}} \tag{14}$$

The limit value δ is called a Feigenbaum constant. Amazingly, the Feigenbaum constant δ is "universal" for all one-dimensional maps f(x), if f(x) has a single locally quadratic maximum. This was conjecture by Feigenbaum, and demonstrated rigorously later on. More specifically, the Feigenbaum constant is universal for one-dimensional maps if the Schwarzian derivative

$$D_{Schwarzian} = \frac{f'''(x)}{f'(x)} - 3/2 \left[\frac{f''(x)}{f'(x)}\right]^2 \tag{15}$$

is negative. You can check that this condition is trivially true for the sine square map. Other examples of maps which are in the same universality class include the Hénon map, Logistic map, Lorenz system, and Navier-Stokes truncations. The value of the Feigenbaum constant can be computed explicitly using functional group renormalization theory. The universal constant also occurs in phase transitions in physics.

A Matlab Code

Below find the Matlab code that was used to generate the figures. If you don't have Matlab, I have tested the code also in octave. It ran without a hitch on my Mac OsX (10.4) using the free and easy to install octave.dmg and gnuplot.dmg files that are available on the web (you need to have installed the free XCode Tools from Apple).

```
% This LaTeX was auto-generated from an M-file by MATLAB.
% To make changes, update the M-file and republish this document.

************ sinsqrcobweb.m *****************

function []=sinsqrcobweb(mu_in,phi_in,x0,N)
%%% MAKES A COBWEB PLOT FOR THE SIN-SQUARE MAP
%%% []=sinsqrcobweb(mu,phi,x0,N)
%%% All arguments optional
%%% mu, phi : parameters in sin-square function
%%% x0 : initial condition (default random)
%%% N  : number of iterations

% glabal variables used to communicate with sinsqrfc
global mu
global phi

% optional input arguments
```

```
if nargin<1
    mu=2.0;            % parameter
else
    mu=mu_in
end
if nargin<2
    phi= pi/4;           % parameter
else
    phi=phi_in;
end
if nargin<3
    x0=rand * pi
    %x0=0.2           % Initial condition
end
if nargin<4
    N=400;            % Number of iterations
end
    x(1) = x0;
    ntrans=300;
for ic=1:ntrans
    x=sinsqrfc(x);
end

% compute trajectory
for ic=1:N
    %x(ic+1) = a*x(ic)*(1-x(ic));
    x(ic+1) = sinsqrfc(x(ic));
end

% ------------------------------------ %
% plot the map function and the line y=x
%clf;
x0 = min(0,min(x)):0.01:max(pi,max(x));
x1 = sinsqrfc(x0); plot(x0,x1); hold on; % Map
%x2 = sinsqrfc(x1); plot(x0,x2); % second iterate
%x3 = sinsqrfc(x2); plot(x0,x3); % third iterate
axis([x0(1) x0(end) x0(1) x0(end)]);
 %set(gca,'XTick',(0:0.1:pi),'YTick',(0:0.1:pi))
 grid on;

 fplot('1*y',[x0(1) x0(end)],'r');

%%%%%% STEP 3: PLOT COBWEB
 line([x(1) x(1)],[0 x(2)],'Color','g')
  plot(x(1), x(1),'ko');
```

```
 for ic=1:N-1
  line([x(ic) x(ic+1)],[x(ic+1) x(ic+1)],'Color','g')
  line([x(ic+1) x(ic+1)],[x(ic+1) x(ic+2)],'Color','g')
  plot(x(ic+1), x(ic+1),'ko');
 end
 line([x(N) x(N+1)],[x(N+1) x(N+1)],'Color','g')

%%%%% STEP 4: SIGN THE PLOT
% at=text(0.1,0.82,['mu=',num2str(mu), ',  \phi=',num2str(phi)]); set(at,'FontSize',12);
ylabel 'x_{n+1}'
xlabel 'x_{n}'
str=['x_{n+1} = f_{\lambda, \phi}[ x_{n} ] = \lambda  sin(x_n + \phi)^2,
\lambda=' num2str(mu) ',  \phi=' num2str(phi) '= \pi/' num2str(pi/phi)];
title(str)
************ end sinsqrcobweb.m *****************

************ bifsinsqr.m *****************
global mu
global phi
%
% Analytics: phi=-pi/4
%
phi= pi/4;

% Period 1 Orbit
x1bif  = 1.184750365923695;
mu1bif = 1.3957652828130325;
x1stbl=0:0.01:x1bif;
mu1stbl = x1stbl./(sin(x1stbl+phi).^2);
x1unstbl = x1bif:0.01:1.5708;
mu1unstbl = x1unstbl./(sin(x1unstbl+phi).^2);

figure(1);clf
hold on
plot(mu1stbl,x1stbl,'b-');
plot(mu1unstbl,x1unstbl,'b--');
plot(mu1bif,x1bif,'bs');

%period 2 orbit
%???

% plotting the bifurcation diagram
r=0:0.01:1.4;

for i=1:length(r);
```

```
    mu=r(i);
    a=0.1;
    for j=1:900
    a=feval(@sinsqrfc,a);
    end;
    a(1)=a;
    for j=2:100
    a(j)=feval(@sinsqrfc,a(j-1));
    end
    rp=mu*ones(1,length(a));
    plot(rp,a,'r.', 'MarkerSize',2)
end;

r=1.4:0.01:pi;
for i=1:length(r);
    mu=r(i);
    a=0.1;
    for j=1:3900
    a=feval(@sinsqrfc,a);
    end;
    a(1)=a;
    for j=2:300
    a(j)=feval(@sinsqrfc,a(j-1));
    end
    rp=mu*ones(1,length(a));
    plot(rp,a,'r.', 'MarkerSize',2)
end;

axis([0 pi 0 pi])
xlabel '\lambda'
ylabel 'x_{n}'
str=['x_{n+1} = f_{\lambda, \phi}[ x_{n} ] = \lambda  sin(x_n + \phi)^2,
\phi=' num2str(phi) '= \pi/' num2str(pi/phi)]
title(str)
************ end bifsinsqr.m *****************


************ sinsqrfc.m *****************
function f=sinsqrfc(x)

global mu
global phi

f= mu .* sin(x+phi).^2;
```

```
end
************ end sinsqrfc.m *****************
```

References

[1] Feigenbaum, M. J., Quantitative Universality for a Class of Non-Linear Transformations., *J. Stat. Phys.* **19**, 25-52 (1978).

[2] Feigenbaum, M. J. , The Metric Universal Properties of Period Doubling Bifurcations and the Spectrum for a Route to Turbulence, *Ann. New York. Acad. Sci.* **357**, 330-336 (1980).

Guidelines for the Optoelectronic experiment

Lucas Illing

1 Intro

The goal is to implement the sine-square map using an opto-electronic device as was first suggested by L. Larger and coworkers [1]. You will investigate the dynamics of the sine-square map in order to learn some basic ideas of nonlinear dynamics and, on the way, you'll learn some things about fiber optics and radio-frequency electronics.

2 Setup

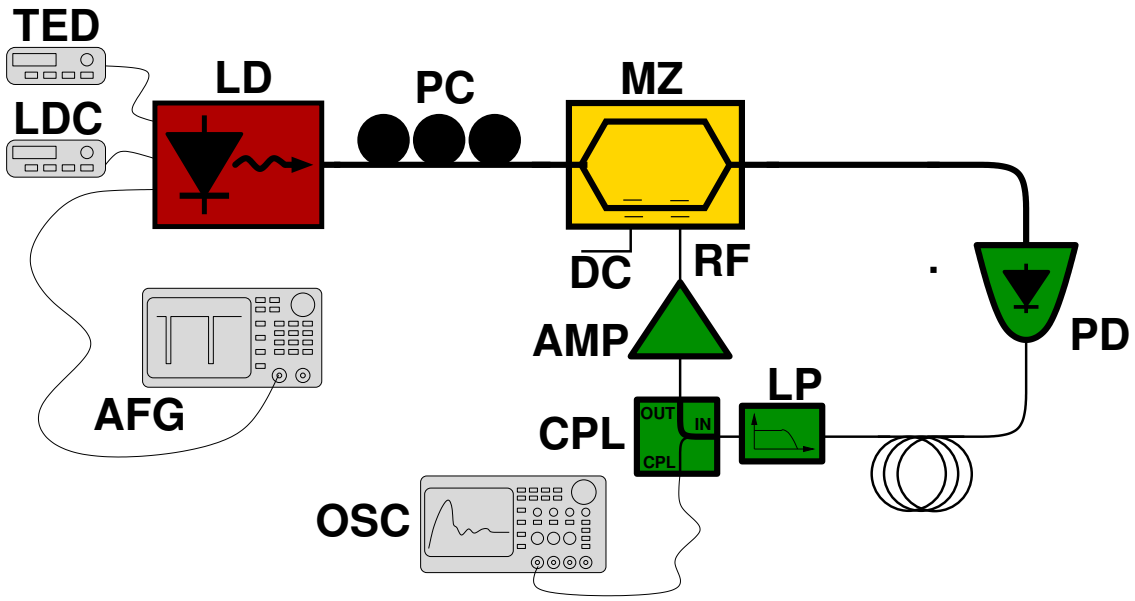

Figure 1: Experimental setup. For details see the text.

The setup is shown in Fig. 1. I consider it in part your job to show that this device does implement (approximately) the map

$$x_{n+1} = \lambda \sin^2(x_n + \varphi) \tag{1}$$

Below I give some hints as to how the device works.

Laser: The laser (LD: Sumitomo SLT 5411-CC) is a fiber pigtailed distributed feedback semiconductor laser working at telecommunication wavelengths (1550nm). Note that this laser can generate more than 50mW of power. This is way more than any of our detectors can handle!

The laser diode is contained in a butterfly package together with a power monitoring diode and temperature control elements. In addition to the DC laser pump current, the laser current can be modulated with high frequency signals (roughly 3GHz). The laser is contained in a butterfly mount (Thorlabs LM14S2) that is connected to the laser temperature controller (TED: Thorlabs TED 200 C), the laser diode current controller (LDC: Thorlabs LDC 205 C), and to an arbitrary function generator (AFG: Tektronix AFG 3251, max. sine-freq 240MHz). The butterfly mount circuitry allows laser modulation signals of up to 500MHz to be passed to the laser.

In the map-experiment the laser will be biased just below the lasing threshold and therefore will be off most of the time. The laser will be turned on for brief periods by a periodic signal of short pulses coming from the AFG.

Task: You need to measure out the laser power versus input current curve. Does the laser threshold agree with the datasheet? Does the output power agree? This measurement will help you determine λ in Eq. (1).

Task: How do you determine the laser output power based on the known AFG-driving voltage? Consult the manual for the laser mount!

Polarization Controller: The ouput light of the laser is polarized. For proper operation of the subsequent Mach-Zehnder Modulator the light has to have a certain linear polarization at the Mach-Zehnder-Modulator input and this polarization is in general different from the one the laser puts out. We use the polarization controller (PC: Thorlabs FPC 560) to optimize polarization.

Task: You will need to optimize the polarization.

Nonlinearity: The Mach-Zehnder Modulator (MZ: JDSU Z-cut) is our nonlinearity. The proportion of the input-light power that makes it through depends in a sine-square fashion on the input voltages of the MZ. You should derive this result yourself, knowing that the input voltage changes the refractive index (in a linear fashion) in one arm of MZ-modulator.

Task: You will need to determine the dependence of the output-light power on the DC-input voltage. The DC input port of the MZ is severely low-pass filtered, therefore, your driving signals should have frequencies well below 10Hz (What are the max. allowed input voltages?). From this measurement the phase φ in Eq. (1) can be determined.

Detectors: We will be using one of two detectors (PD) depending on the experimental task: either the "slow" Thorlabs (2011) detector or the "fast" Miteq (DR-125G-A) detector. These photodiode-plus-amplifier devices convert light power to an electrical signal.

You need to familiarize yourself with these detectors. The most important information you should obtain is: what is the gain of the detector; what is the bandwidth of the

detector (low and high freq. cutoffs); and what is the maximum power that the detector can handle!

Task #1: Make sure you understand the maximum allowed power the detectors can handle and how to ensure that you never exceed these values in this experiment. You need to demonstrate to me that you know how to do this before you can make any measurements.

Task: You might also want to know how much power reaches the detector. In other words how much power do you lose between your laser output and the detector input. Again, this will help you quantify λ

The coaxial delay line is the main contribution to the feedback delay. Note, the total feedback delay has to match the period of the pulses from the arbitrary function generator that are used to turn on and off the laser.

Task: Measure the total feedback delay. Does this agree with your expectation based on the cable length?

Low Pass Filter: We low pass filter the signal with an element we know, instead of relying on not well known low pass filter effects due to the slow response time of device elements such as the butterfly mount. I think we can also take this out without changing the results. You might try this.

Directional Coupler: At the CPL-port the directional coupler (CPL: MiniCircuits ZDFC-20-5-S+, 0.1-2000 MHz) couples out a signal that is -20dB (nominally 19.5dB) of the feedback signal. The feedback signal (OUT-port) experiences a nominal loss of 0.7dB.

Task: What does a 20dB loss mean in terms of peak to peak voltages? in other words, how do you interpret the voltages that are measured on the oscilloscope?

Modulator Driver: The JDSU H301 modulator driver (AMP) with a bandwidth > 10GHz amplifies the feedback signal with typical amplitudes of hundreds of millivolt to several volt.

Possible task: If you have time you might consider measuring the modulator driver. You will find that it does not behave like a perfectly linear amplifier. You might want to include this information in an improved model.

Fiber Connectors: Our fibers are single mode SMF-28 optical fibers and they can be connected to each other using simple "plugs", the fiber connectors. The fiber connectors come in different types and can be distinguished by color and shape. *The connector-types have to match!*

The connectors with screw-in metal jacked are called *FC* (fixed connector). The FC-connectors with green protective jacket and cap are *FC-APC* connectors, where *APC* stands for angle-polished physical contact and describes a specification where the fiber end is polished to 8°. This connector type combines low connector loss with minimal back-reflection. The FC connectors with a white protective jacket and a yellow cap are *FC-PC* connectors. They are polished flat at the end.

3 Map Dynamics

The main goal is to measure a bifurcation diagram and check that it roughly agrees with the predicions of the map model.

References

[1] Larger, L., Lacourt, P. A., Poinsot, S. and Hanna, M., From flow to map in an experimental high-dimensional electro-optic nonlinear delay oscillator, *Phys. Rev. Lett.* **95** 043903 (2005).